Hindawi
Advances in Materials Science and Engineering
Volume 2021, Article ID 8288648, 13 pages
https://doi.org/10.1155/2021/8288648

Research Article

Bearing Capacity of Concrete Filled Steel Tube Circular Arch under the Six-Point Uniformly Distributed Loading and Its Engineering Application

Keming Liu and Xizhen Sun

School of Civil Engineering and Architecture, Linyi University, Linyi 276000, China

Correspondence should be addressed to Xizhen Sun; 496661950@qq.com

Received 29 October 2021; Accepted 22 November 2021; Published 13 December 2021

Academic Editor: Xin Cai

The influence of rise-span ratio on the bearing performance of concrete filled steel tube (CFST) circular arch was studied in this paper, three groups of CFST circular arch specimens with different rise-span ratios (0.154, 0.207, and 0.26) were selected, the six-point uniformly distributed loading was performed, and bearing performance experiments on CFST circular arch specimens with fixed ends were carried out. In this study, the ultimate bearing capacity and deformation failure characteristics of CFST circular arch specimens were obtained. The comparative analysis shows that the deformation evolution of CFST circular arch specimens has experienced compaction stage, elastic stage, elastic-plastic stage, and plastic stage. In the elastic-plastic and plastic deformation stages, the circular arch shows good ductility and bearing capacity. The bearing capacity of the circular arch is significantly affected by the rise-span ratio. Compared with circular arch specimens with a rise-span ratio of 0.154, the yield load of specimens with a rise-span ratio of 0.207 and 0.26 is increased by 50.8% and 61.5%, and the ultimate bearing capacity is increased by 42.7% and 68.3%, respectively. The larger the rise-span ratio, the greater the yield load and ultimate bearing capacity of the specimen and the stronger the deformation resistance of circular arch. The numerical simulation on the bending resistance process of circular arch was performed by ABAQUS to present the compression failure process of steel tube and core concrete. The simulation results are in good agreement with the experimental results. The experimental and simulation results show that the circular arch first yields at the inner side of the arch foot, and the curvature of different positions of the specimen is no longer consistent. When the ultimate bearing capacity is reached, the steel pipe at the arch foot obviously heaves, and the hooping effect of the steel pipe on the concrete is invalid. Based on the above research results, a closed composite support scheme of "bolt mesh shotcrete + vertical elliptical CFST support + steel fiber concrete shotcrete layer + reinforced anchor cable" was proposed for the extremely soft rock roadway and successfully applied in the Qingshuiying coal mine.

1. Introduction

Concrete filled steel tube (CFST) structure can make full use of the hoop effect of steel tube and the good bearing performance of core concrete. The symbiosis of steel tube and core concrete in mechanical properties greatly increases the strength and bearing capacity. The CFST structure has been widely used in the ground building, and a series of research results of CFST members have been obtained [1–12]. Based on the mechanical properties of steel-concrete composite materials, underground cast-in-place CFST support is invented as high-strength support, which is suitable for the support of deep roadway and soft rock roadway. Under the same amount of steel, its bearing capacity can reach about 3 times that of U-shaped steel support [13]. The supports are connected by connecting rods, which have a high deformation resistance and superior plastic and seismic performance. At present, this support has been successfully applied in more than 20 coal mines in China, including the deep roadway, soft rock roadway, and roadway intersection point [14–23].

The performance research of CFST structure in deep underground engineering mainly focuses on two aspects:

axial compression bearing capacity and flexural capacity. Li Xuebin [24], Wang Jun [25], and others studied the mechanical properties of steel-concrete short columns with different wall thicknesses and inner diameters of steel tube. Qu Guanglong [26] compared and tested the flexural bearing capacity of different groups of CFST straight beam specimens. Wang Bo [13], Liu Guolei [27], and Wang Jun [25] studied the mechanical properties of CFST supports in different specifications under concentrated load and improved the overall bearing capacity of the support by welding bending round steel on the tensile side of the support. The development of CFST support technology has been promoted by a large amount of experimental data and results.

The traditional CFST support is spliced by 4–6 circular arches. In this study, circular arch columns were selected, which are more reasonable than short columns and straight beams for research. Generally, the bearing performance of circular arch members is affected by the rise-span ratio, the strength of core concrete, the content of steel fiber, the thickness of steel pipe wall, the diameter of steel pipe, and the size of bending round steel. Under the condition of uniformly distributed loading and complete fixation of arch foot, He Xiaosheng [28] studied the ultimate bearing capacity of CFST circular arch specimens with different pipe diameters, wall thickness, and welded bending round steel, monitored the displacement at the span and arch foot, and analyzed the deformation characteristics of CFST circular arch specimens. In the previous studies on CFST members, the steel content of the members (such as pipe diameter, wall thickness, and bending round steel) is mainly studied as influencing factor of the bearing performance. The basic conclusion is that increasing the steel content can improve the bearing capacity and deformation performance of CFST members. However, increasing the steel content undoubtedly increases the economic cost. In this study, the influence of the rise-span ratio on the bearing performance of CFST circular arch specimens was mainly studied, and the research results were taken as an important reference basis for the section design of CFST support. Finally, the composite support scheme of CFST support was proposed and successfully applied to the support engineering of a large section roadway. This study provides successful methods and experience for the support of soft rock roadway in a deep mine.

2. Experiment on Bearing Capacity of CFST Circular Arch Specimens

2.1. Experimental Purpose

(1) The six-point uniformly distributed loading and three different rise-span ratios were selected to test the ultimate bearing capacity of CFST circular arch specimens under the constraint of fixed support at both ends.

(2) The failure modes of CFST circular arch specimens with different rise-span ratios were compared and analyzed.

(3) The mid-span displacement of CFST circular arch specimens with different rise-span ratios was monitored, and the load-displacement curves were drawn for comparative analysis.

2.2. Design and Fabrication of CFST Circular Arch Specimens

2.2.1. Design and Fabrication of CFST Circular Arch Specimens. The Φ 140×6 mm type seamless steel pipe was selected as the main steel pipe for CFST circular arch specimens. Within the range of rise-span ratio in the engineering application, according to the symmetry of structure and load, CFST specimens with the rise-span ratio of 0.154, 0.207, and 0.26 were employed. The strength grade of core concrete was proportioned as C40, and the restraint form of the specimen end was fixed restraint. A total of 3 CFST circular arch specimens were tested. Table 1 shows the design parameters and specifications of CFST circular arch specimens with different rise-span ratios. Figure 1 shows the specific specifications of CFST circular arch specimens.

2.2.2. Specimen End Treatment. After the core concrete was completely hardened, the steel plate was welded at the end of the specimen as the end restraint. The end restraint not only increased the force area of the end face but also fit better with the supporting inclined plate of the support, which significantly enhanced the stability and the bearing capacity of the specimen. At the same time, it is convenient to observe the damage of arch foot position.

2.3. Experimental Scheme Design. The compression bending performance test of CFST circular arch specimens was carried out in the Structural Laboratory of the School of Civil Engineering, Shandong Jianzhu University. The laboratory is equipped with a large reaction frame test bench and jacks of different tonnage, which has the experimental conditions and can meet the experimental requirements. In this experiment, displacement monitoring was performed to monitor the vertical displacement of mid-span of the circular arch. Figure 2 shows the loading photos after actual manufacturing.

2.4. Experimental Procedures

(1) The circular arch specimen was assembled on the ground and pasted with the strain gauge.

(2) The support was hoisted to the experimental platform, the plane restraint support beam was stalled, and the strain gauge wire was connected. Then the displacement sensor was installed, and the hydraulic jack was adjusted to make it in the same vertical loading plane as the support.

(3) Preloading. The preloading was used to eliminate the virtual displacement of the whole loading device and ensure that all parts were in full contact and work together. Before preloading, the readings of each instrument were recorded, and then preloading was performed on the specimen, The applied load shall not exceed 10% of the maximum load. The

Table 1: Parameters of CFST circular arch specimens with different rise-span ratios.

Specimen no.	Pipe diameter/mm	Thickness/mm	Concrete strength grade (MPa)	Rise-span ratio	End constraint
1	140	6	C40	0.154	
2	140	6	C40	0.207	Fixed constraint
3	140	6	C40	0.26	

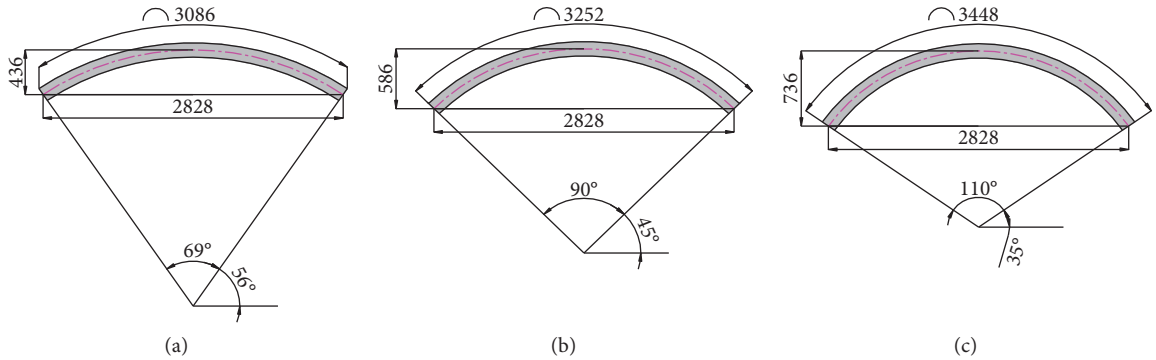

Figure 1: Schematic diagram of circular arch specimens with different rise-span ratios. (a) 0.154. (b) 0.207. (c) 0.26.

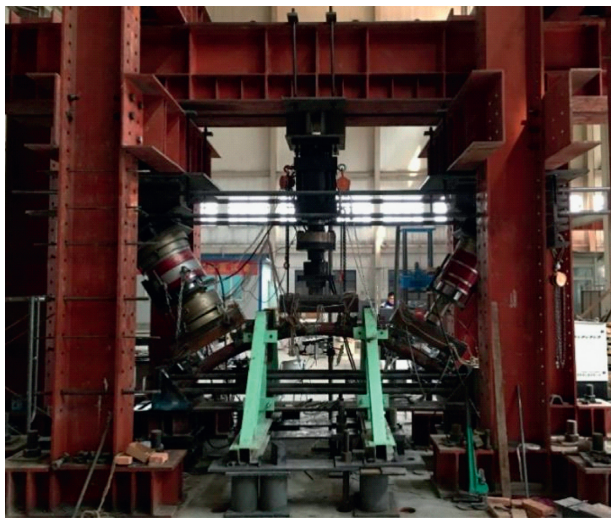

Figure 2: Test bench and loading scheme.

preloading plan was divided into three levels: 20 kN, 40 kN, and 60 kN.

(4) Formal loading. The maximum bearing capacity of the circular arch specimen was estimated to be in the range of 700–1300 kN through theoretical calculation. The static graded loading mode was adopted in the experiment, and the circular arch specimen was loaded in 10–20 levels. Before reaching 60% of the estimated load value, the loading was increased by 100 kN per level; when 60%–80% of the estimated load value was reached, the loading was increased by 20–50 kN per level; after exceeding 80% of the estimated value, the loading was increased by 10 kN per level. After the yield of the circular arch specimen, the loading method was changed into displacement control, and the reading was recorded once per second. The continuous loading time of each level was about 1–2 min, and the measured data were recorded after the stable deformation of the specimen.

(5) Work after loading. When the circular arch specimen was obviously yielded and fully deformed, the loading was terminated and the jack was withdrawn. The experimental test instrument was first removed, followed by the distribution beam and loading cushion block. The horizontal restraint device and the specimen on one side were removed eventually.

2.5. Analysis of Experimental Results

2.5.1. Load-Displacement Analysis of Circular Arch. The load-displacement relationship at the mid-span position of three circular arch specimens with different rise-span ratios is obtained, as shown in Figure 3.

According to the load-displacement curves, the deformation of circular arch specimens can be divided into four stages: compaction stage, elastic deformation stage, elastic-plastic deformation stage, and plastic deformation stage.

(1) Compaction deformation stage. This stage starts from the moment of loading and is presented as the concave section at the beginning of the curve. In this stage, due to the loading of the jack, the small gap between the circular arch and the steel member of the base is compacted, and the circular arch produces a small settlement downward as a whole, contributing a part of the displacement. At the same time, under the six-point uniformly distributed loading, the stress of circular arch is dominated by axial force, similar to CFST short column. At the initial stage of loading, the transverse deformation of steel is greater than that of concrete, and the two work

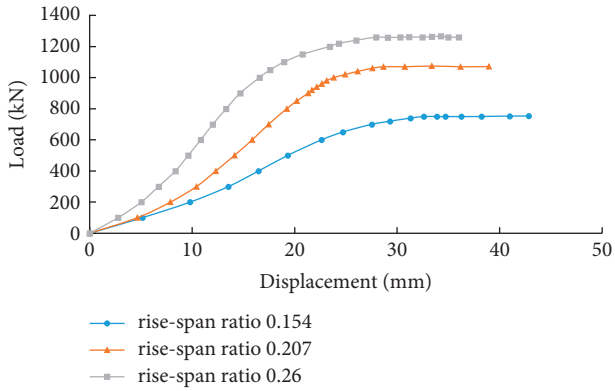

Figure 3: Load-displacement curves of circular arch specimens with different rise-span ratios.

independently. The early deformation of steel pipe is reflected in the vertical displacement monitored by the displacement meter; under axial force, internal pores and gaps of the core concrete are gradually compacted.

(2) Elastic deformation stage. This stage is presented as the linear relationship between load and displacement in the curve.

(3) Elastic-plastic deformation stage. When the applied load exceeds the yield load of the circular arch, the slope of the curve decreases steadily and monotonically with the increase of the load, and the deformation of the circular arch shows a nonlinear growth trend.

(4) Plastic deformation stage. This stage is presented as the straight section in the curve, which is the ideal plastic state. The CFST circular arch member has good ductility and bearing capacity.

As shown in Figure 3, the greater the rise-span ratio, the greater the ultimate bearing capacity of circular arch. The ultimate bearing capacity of circular arch specimens with a rise-span ratio of 0.154, 0.207, and 0.26 can reach 753 kN, 1074.3 kN, and 1267.1 kN, and the corresponding mid-span displacement is 40.98 mm, 33.37 mm, and 34.26 mm, respectively. It shows that these CFST circular arch specimens have the high bearing capacity and strong deformation capacity.

2.5.2. Bearing Capacity Analysis of Circular Arch Specimens. The yield load, ultimate bearing capacity, and corresponding mid-span displacement of circular arch specimens are summarized in Table 2. The histogram of yield load and ultimate load of three circular arch specimens is shown in Figure 4.

According to Table 2 and Figure 4, the following can be concluded:

(1) The bearing capacity of circular arch in-plane is significantly affected by the rise-span ratio. The larger the rise-span ratio, the greater the yield load and ultimate bearing capacity. Compared with circular arch specimens with a rise-span ratio of 0.154, the yield load of specimens with a rise-span ratios of 0.207 and 0.26 is increased by 50.8% and 61.5%, and the ultimate bearing capacity is increased by 42.7% and 68.3%, respectively.

(2) For the shallow arch with a rise-span ratio of 0.154 and 0.207, the ultimate bearing capacity of the specimen is increased by 15.8% and 9.6% compared with its yield load, while the ultimate bearing capacity of the specimen with a rise-span ratio of 0.26 is increased by 20.7% compared with its yield load.

(3) The larger the rise-span ratio, the smaller the deformation required for the specimen yield and reaching the ultimate bearing capacity. It indicates that the circular arch specimen with a large rise-span ratio has greater stiffness. In other words, increasing the rise-span ratio can make the circular arch have strong deformation resistance.

2.5.3. Analysis of Deformation and Failure Characteristics of Circular Arch Specimens. The experimental results show that the specimens with different rise-span ratios yielded first at the inner side of the arch foot. After that, the curvature at different positions of the circular arch was no longer the same, and the arch foot began to bear the combined action of compression and bending. With the further increase of the load, the cracks in the core concrete gradually penetrated and expanded, and the concrete volume increased rapidly with the outward expansion. As a result, the circular section of the steel pipe cannot be maintained, and the hooping effect on the core concrete was gradually weakened until the bearing capacity of the specimen was lost. Figure 5 shows the deformation and failure at the arch foot. The significant bulging and thickening of steel pipes at the arch feet at both ends can be observed. At this time, the axis of the circular arch is not perpendicular to the plane of the welded end plate.

Figure 6 shows the overall deformation and failure of the specimen. It can be seen that the curvature radius of circular arch specimens with different rise-span ratios increases. The larger the rise-span ratio is, the higher the deformation degree is and the more the arc tends to a straight line.

After the experiment, the outer wall of the steel pipe at the arch foot was cut and the damage of the core concrete was observed, as shown in Figure 7. The core concrete away from the arch foot has good integrity and no obvious cracks. The core concrete at the arch foot is destroyed along the inclined section at an angle of approximately 45° to the arch axis, which belongs to typical shear dilatancy failure. The greater the rise-span ratio, the worse the integrity.

3. Single-Factor Finite Element Analysis of Rise-Span Ratio

The indoor experiment can only monitor the bearing capacity, displacement, strain, and other parameters of the circular arch. The numerical simulation is needed for the monitoring of the stress distribution, axial force, and

Table 2: Bearing capacity of circular arch specimens with different rise-span ratios.

Specimen no.	Rise-span ratio	Yield load (kN)	Corresponding displacement (mm)	Ultimate load (kN)	Corresponding displacement (mm)
1	0.154	650	24.68	753	40.98
2	0.207	980	23.11	1074.3	33.37
3	0.26	1050	17.61	1267.1	34.26

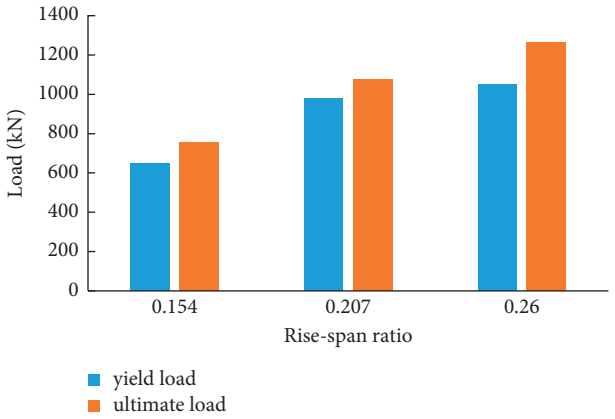

Figure 4: Schematic diagram of bearing capacity of circular arch specimens with different rise-span ratios.

(a) (b) (c)

Figure 5: Schematic diagram of arch foot failure of specimens with different rise-span ratios. (a) 0.154. (b) 0.207. (c) 0.26.

(a) (b)

(c)

Figure 6: Overall deformation of circular arch specimens with different rise-span ratios. (a) 0.154. (b) 0.207. (c) 0.26.

(a) (b) (c)

Figure 7: Cracking of core concrete of specimen with different rise-span ratios. (a) 0.154. (b) 0.207. (c) 0.26.

bending moment in the circular arch. In this study, ABAQUS software was used to analyze the stress, axial force, bending moment, and load-displacement curve in CFST circular arch with different rise-span ratios.

3.1. Mechanical Model Establishment and Boundary Constraints. The establishment of the finite element model was consistent with the actual situation of the experiment. The six-point uniformly distributed loading was performed along the arch axis of the steel pipe, and the end of the specimen was fixed and restrained in the normal direction to restrict the out-of-plane deformation of the specimen. Figure 8 shows the mechanical model of the specimen. Compared with the experimental loading, the computer simulation can load the specimen more stably. Therefore, within the loading range of 0–400 kN, the load on the cushion block was increased by 50 kN per level; above the loading of 400 kN, the load on the cushion block was increased by 25 kN per level.

3.2. Element Selection and Grid Division. The accuracy of finite element simulation depends strongly on the type of element used. In the elastic-plastic simulation analysis of CFST circular arch, the displacement and strain of circular arch are large, and the circular arch bears the action of bending moment; then the complete integral element is easy to produce volume self-locking phenomenon; therefore, the primary reduced integral element (C3D8R) is selected as the simulation element type.

3.3. Constitutive Selection of Steel Pipe and Concrete. Table 3 shows parameter setting in the plastic damage model of steel pipe.

Table 4 shows the parameter settings in the concrete plastic damage model. The selection of main parameters was based on [29].

3.4. Simulation Results and Analysis

3.4.1. Load-Displacement Curve Analysis. Figure 9 shows the load-displacement curves of circular arches with different span ratios at their ultimate bearing capacity. Due to the idealized finite element simulation process, the deformation of circular arch has only three stages: elastic stage, elastic-plastic stage, and plastic deformation stage. As shown in Figure 9, the ultimate bearing capacity of the circular arch with the rise-span ratio of 0.154, 0.207, and 0.26 is 750 kN, 1030 kN, and 1280 kN, respectively. The maximum error with the experimental value is controlled within 5%, indicating that the simulation effect is effective. At this time, the corresponding mid-span displacement is 37.9 mm, 37 mm, and 35.1 mm, respectively. It can be seen that the greater the rise-span ratio, the higher the ultimate bearing capacity of the circular arch and the stronger the ability to resist bending deformation. For the deep arch with a rise-span ratio of 0.26, the bearing capacity of the circular arch can still be greatly improved after yield, which is consistent with the experimental result.

3.4.2. Stress Distribution Analysis of Circular Arch. After the circular arch with a rise-span ratio of 0.154, 0.207, and 0.26 reaches the ultimate bearing capacity, the stress distribution of steel pipe and concrete is obtained, as shown in Figures 10–12. The following is concluded:

(1) Under the six-point uniformly distributed loading mode, there is only a compressive stress area and no tensile stress area in the circular arch.

(2) For circular arches with different rise-span ratios, the stress on the steel pipe surface is greater than that in the core concrete.

(3) The stress distribution of the outer wall of the steel tube and the inner part of the core concrete has a large jump. On the whole circular arch, the circular section of the CFST in contact with the loading cushion block bears the least stress, the circular section between the adjacent cushion blocks bears higher stress, and there is a stress reduction area in the loading area of the middle two cushion blocks.

3.4.3. Comprehensive Displacement Analysis of Circular Arch. Figure 13 shows the comprehensive displacement nephogram of circular arch with different rise-span ratios when it reaches the ultimate bearing capacity. Under the six-point uniformly distributed loading mode in the experiment, the deformation of the circular arch is symmetrical. From the arch foot to the middle of the span, the comprehensive displacement of the circular arch gradually increases. Besides,

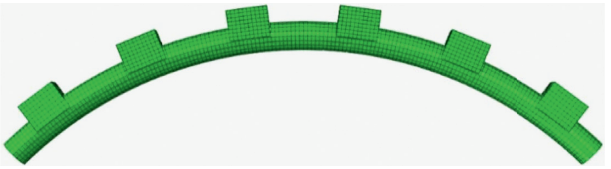

Figure 8: Mechanical model of circular arch.

Table 3: Parameters of elastic-plastic damage model of seamless steel tube.

Density (kg·m^{-3})	Elastic modulus (GPa)	Poisson's ratio	Yield strength (MPa)	Ultimate strength (MPa)
7800	206	0.3	245	410

Table 4: Parameters of concrete plastic damage model.

Density (kg·m^3)	Elastic modulus (GPa)	Poisson's ratio	Dilatancy angle (°)	Flow potential eccentricity	Ratio of biaxial isobaric strength to uniaxial strength	Second stress ratio	Viscosity coefficient
2400	33	0.2	30	0.1	1.16	0.66667	0.0005

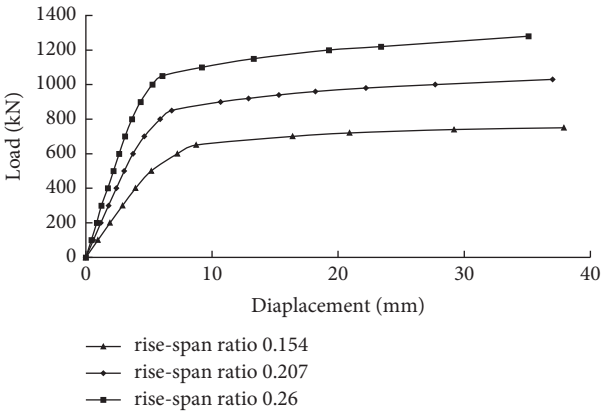

Figure 9: Load-displacement curves of circular arch with different rise-span ratios.

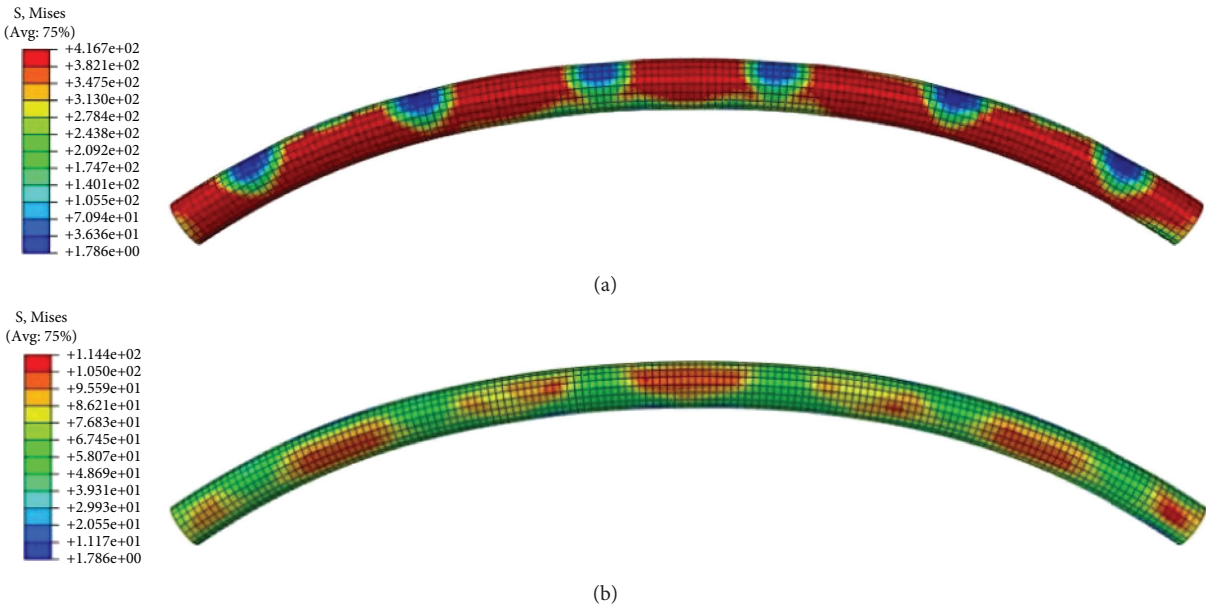

Figure 10: Stress nephogram of circular arch with a rise-span ratio of 0.154. (a) Stress nephogram of steel pipe. (b) Stress nephogram of core concrete.

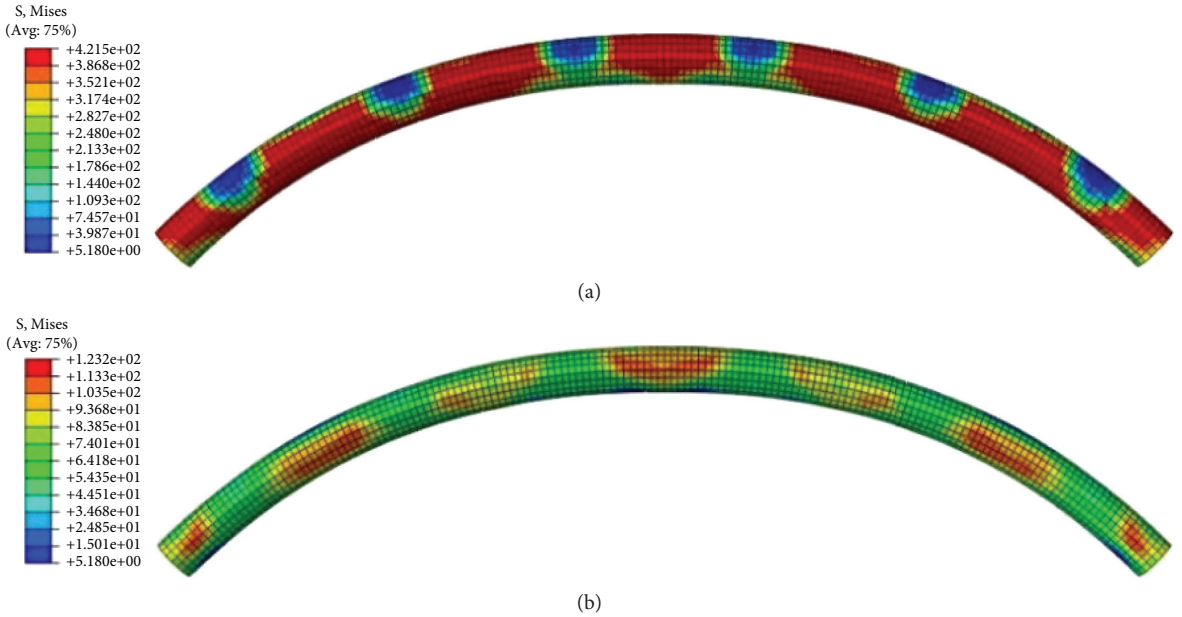

Figure 11: Stress nephogram of circular arch with a rise-span ratio of 0.207. (a) Stress nephogram of steel pipe. (b) Stress nephogram of core concrete.

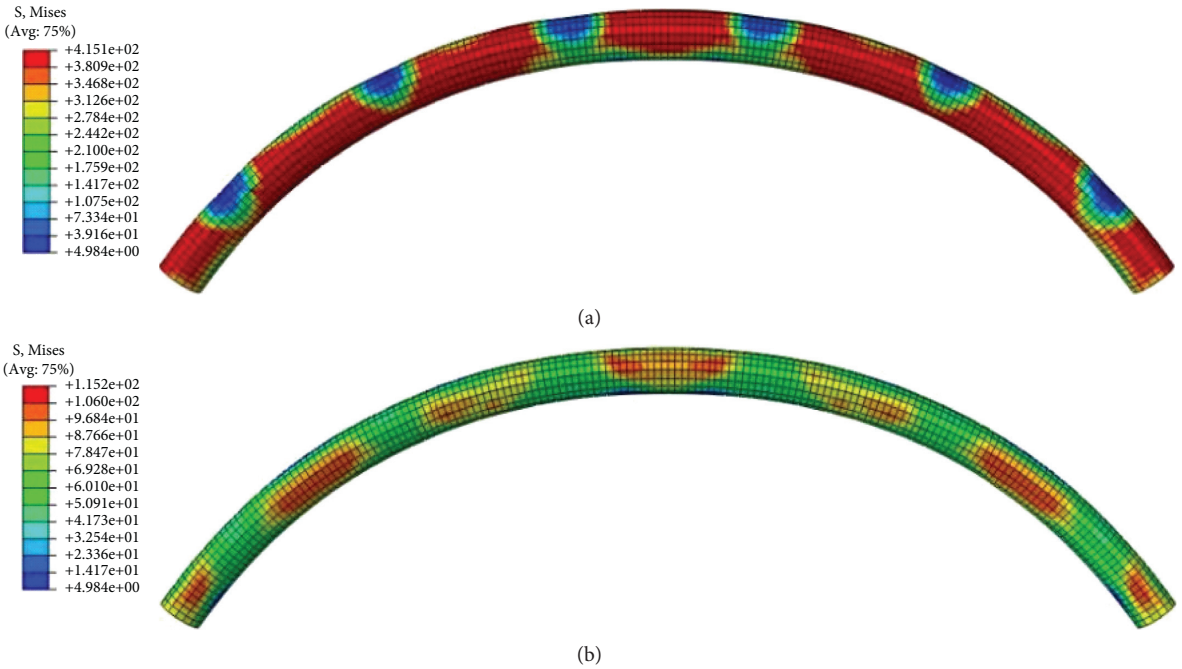

Figure 12: Stress nephogram of circular arch with a rise-span ratio of 0.26. (a) Stress nephogram of steel pipe. (b) Stress nephogram of core concrete.

the smaller the rise-span ratio, the larger the comprehensive deformation and range at the middle of the span.

3.4.4. Analysis of Axial Force and Bending Moment of Circular Arch. The deformation and stress of circular arch with different rise-span ratios are symmetrical. Therefore, a half-span circular arch is taken, and 15 monitoring points are set successively from the mid-span section to the end of arch foot section to monitor the axial force and bending moment in the half-span circular arch. The monitoring curves of axial force and bending moment of circular arch with different rise-span ratios in elastic stage (taking 500 kN as an example) and after reaching its ultimate bearing capacity are obtained, as shown in Figures 14 and 15.

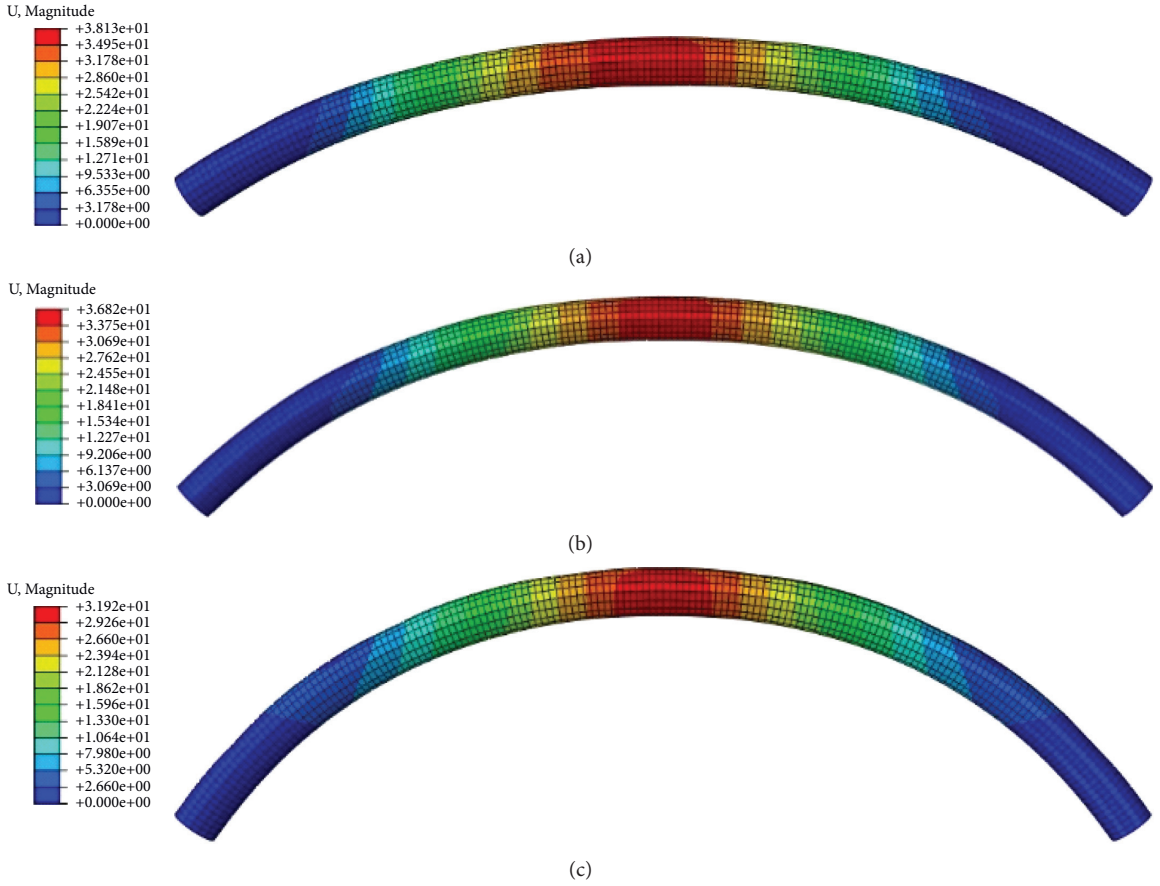

Figure 13: Comprehensive displacement nephogram of circular arch with different rise-span ratios. (a) 0.154. (b) 0.207. (c) 0.26.

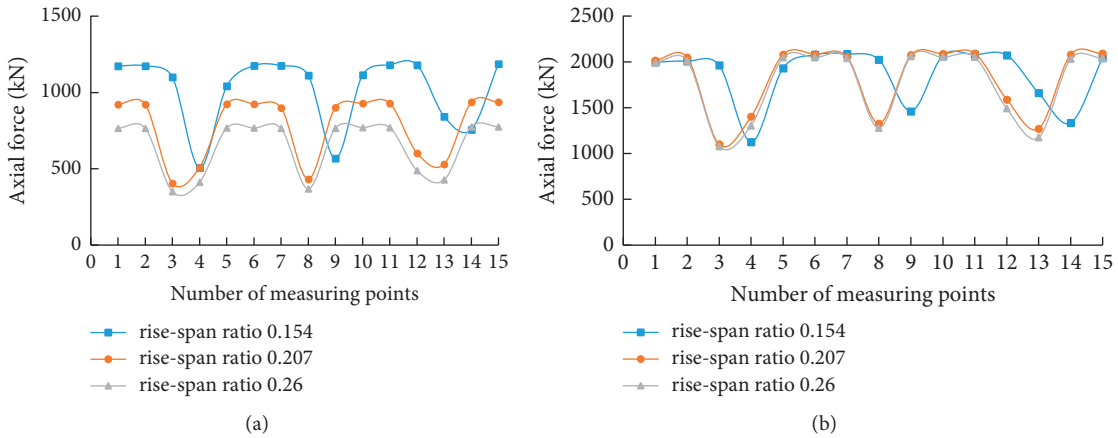

Figure 14: Axial force monitoring of half-span circular arch with different rise-span ratios. (a) Under the load of 500 kN. (b) At the ultimate bearing capacity.

In Figure 14, the three concave sections in each curve correspond to the location of the cushion block in the circular arch, and the straight section between the two adjacent concave sections corresponds to the circular arch section between the adjacent cushion blocks. The following can be seen:

(1) Under the same load, the smaller the rise-span ratio, the greater the axial force in the circular arch; after reaching the ultimate bearing capacity, there is no obvious difference in the axial force of the circular arch.

(2) The axial force distribution in the circular arch is jumping. The axial force of the circular arch in the contact area with the cushion block is small, and there is no obvious change in the axial force in the circular arch between adjacent cushion blocks.

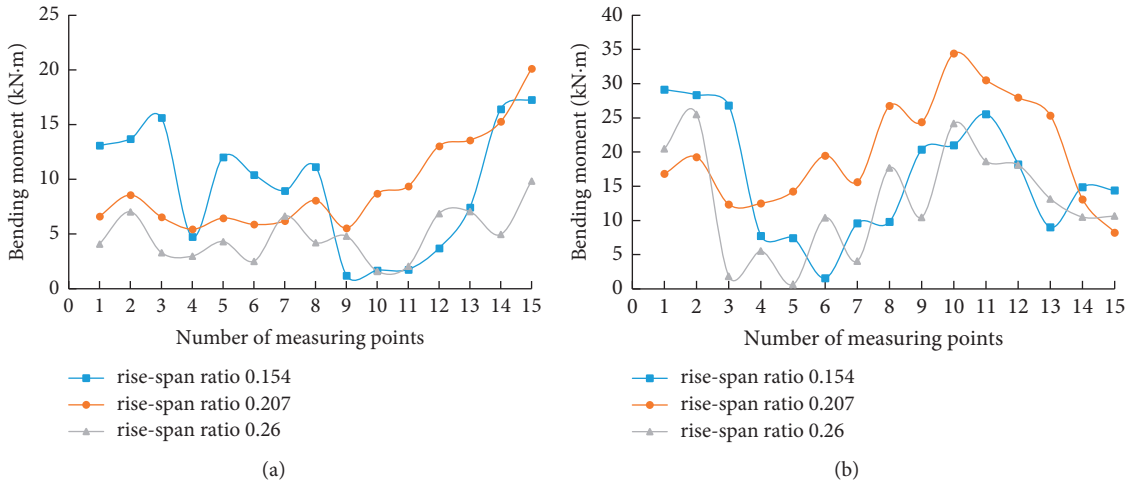

Figure 15: Bending moment monitoring diagram of the half-span circular arch with different rise-span ratios. (a) Under the load of 500 kN. (b) At the ultimate bearing capacity.

As shown in Figure 15, the following can be seen:

(1) The bending moment in the circular arch changes greatly, especially near the cushion block. Taking the circular arch with a rise-span ratio of 0.154 as an example, points 3, 4, 8, 9, 13, and 14 are the monitoring points in the circular arch under the cushion block, and the bending moment changes most obviously near these points.

(2) In the elastic deformation stage, the smaller the rise-span ratio, the larger the bending moment in the circular arch and the worse the bending resistance. The maximum bending moment of the circular arch with different rise-span ratios appears at the arch foot. Combined with the axial force monitoring diagram, it can be seen that the bending moment and axial force at the arch foot are the largest, and the circular arch yields at the arch foot first.

(3) When the load value reaches the ultimate bearing capacity of the circular arch, the bending moment at the arch foot of all circular arches decreases, and the maximum bending moment appears in the middle of span or near 1/4 span.

4. Engineering Application

4.1. Engineering Background. The buried depth of the horizontal temporary sump (+786 m) of the auxiliary shaft in the Qingshuiying coal mine was 596 m and was mainly arranged in the floor of the 2# coal seam. The surrounding rock of the roadway was mainly argillaceous cemented sandstone with developed bedding and joints, which was soft and easily weathered. The lateral pressure coefficient in this area was 1.45 and the formation dip angle was 20°–26°. The mechanical and hydraulic properties of the surrounding rock were tested by field sampling. The natural uniaxial compressive strength of rock was 5.1–12.9 MPa, the saturated uniaxial compressive strength was 3.6–5.3 MPa, and the softening coefficient was 0.18–0.2. The porosity of the rock was 11%–16%, the water absorption was 22%–27%, and the expansion rate was 20.7%–36.7%. The content of clay minerals in the surrounding rock of the roadway was high, with a relative content of 46.2%, and the content of montmorillonite in the clay minerals was more than 30%. The rock softening coefficient was less than 0.2, and the expansibility and water absorption softening were significant. Therefore, the surrounding rock belongs to a typical strong expansion extremely weak rock stratum.

The original section of the temporary sump roadway was a straight wall semicircular arch, and the combined support form of "bolt mesh shotcrete + concrete shotcrete layer + U36 steel support" was adopted for the support, and the specification of anchor rod was Φ 22 mm × *L*2500 mm, with a row spacing of 800 mm × 800 mm; the thickness of concrete shotcrete layer was 300 mm. The spacing between U36 steel supports was 800 mm. After 20 days of roadway excavation and support, the slurry skin on the lap area of the circular arch and straight wall section cracked and fell off; the two sides of the shotcrete layer cracked and bulged out rapidly, and the delamination subsidence of the roof in some sections exceeded 500 mm; the floor heave was strong, and it reached 1400 mm in some sections. As a result, the roadway was finally unstable and damaged.

4.2. Cause Analysis of Roadway Deformation and Failure. The main causes of roadway deformation and failure were as follows:

(1) The surrounding rock had low strength and was affected by water.

(2) The influence of tectonic stress was significant. The convergence of the two sides of the roadway increased linearly with the lateral coefficient, and the floor heave also increased.

(3) The roadway section was large, the support strength was low, and the section and support design were unreasonable.

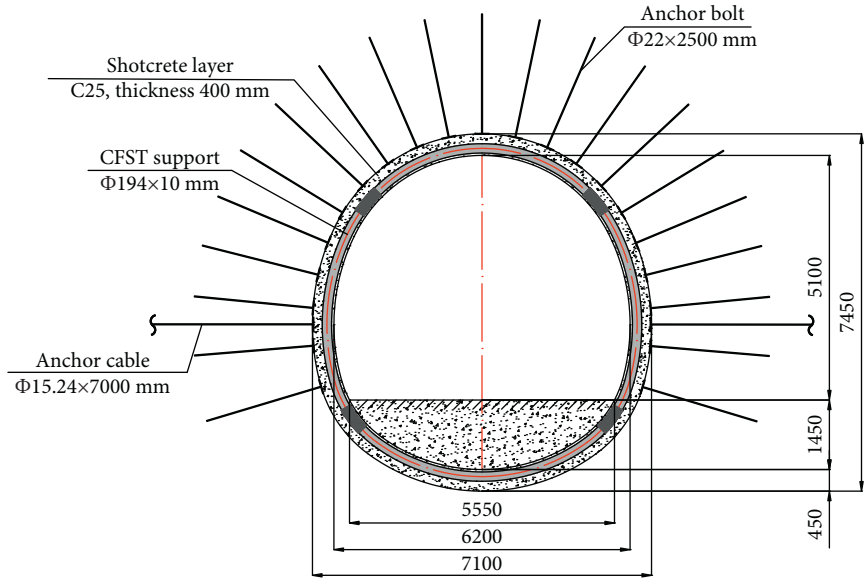

Figure 16: Composite support schematic (unit: mm).

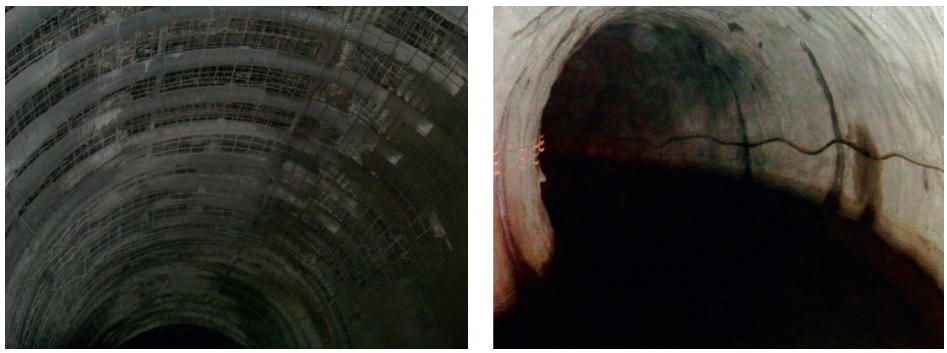

(a) (b)

Figure 17: Supporting effect graph. (a) Arranging CFST support in the early stage; (b) usage as a temporary sump for 2 years.

(4) The deformation of key parts was large, and the deformation was mainly the movement of roof and floor; the large deformation of key parts drove the overall deformation and instability of the roadway.

4.3. Composite Support Scheme of CFST Support. By analyzing the causes of deformation and failure of surrounding rock in the roadway, the following measures were put forward:

(1) High prestressed bolts were used to strengthen the rock mass within a certain width around the roadway, and the influence ranges between bolts were superimposed to form a continuous high-stress compression arch to restrain the convergence deformation of the external surrounding rock.

(2) The metal support was changed into closed CFST support, which was designed as a vertical ellipse. The roadway was dominated by the surrounding rock deformation of the roof and floor. Referring to the conclusion of the circular arch experiment, the rise-span ratio of the circular arch at the top and bottom was increased to improve its bending resistance and bearing performance, so as to restrain the large deformation in the vertical direction. The use of an arc section can improve the stress state of surrounding rock at the same time.

(3) The mechanical properties and stress state of the shotcrete layer were improved, and the integrity of the shotcrete layer was maintained. Two layers of reinforcement mesh were set in the shotcrete layer to improve its toughness. The high-strength radial support force provided by the support and the external surrounding rock pressure made the shotcrete layer in a three-dimensional stress state, and the stress state of the shotcrete layer can be significantly improved.

The final support scheme was as follows: the original roadway was expanded and repaired, and anchor mesh spray was used for the initial support, and then "CFST

support + steel fiber concrete shotcrete layer + reinforced anchor cables by 2 supports" was used for secondary support. The Φ 194 mm × 10 mm seamless steel pipe was selected as the main steel pipe of support. The core concrete in the steel pipe was proportioned as C40. The thickness of the concrete shotcrete layer was 50 mm, the thickness of the shotcrete layer was 400 mm, and the strength grade was C25. The anchor bolt of Φ 22 mm × L2500 mm left-hand threaded steel bolt without longitudinal reinforcement was used, with a row spacing of 700 mm × 700 mm. The specification of the anchor cable was Φ 15.24 mm × L7000 mm, with a spacing of 700 mm.

The overall design of the composite support scheme is shown in Figure 16.

4.4. Monitoring of Surrounding Rock Deformation. The steel-concrete support section of the temporary water storage was 64 m long, and 92 supports were used in total. The cross point method was used, and the displacement of two sides, roof and floor, of one section was tested every 10 supports. The convergence deformation of surrounding rock in different sections can be divided into rapid deformation, slow deformation, and smooth deformation stages. Within 15 days of support, the surrounding rock deformation was relatively strong. Within 15–30 days of support, the deformation speed slowed down gradually. After 30 days of support, the deformation growth was not obvious. It indicates that the convergence deformation of roadway has been effectively controlled. The control effect on the floor heave is significant, and the maximum deformation of surrounding rock is less than 100 mm. Figure 17 shows the supporting effect of the roadway at different stages. It can be seen through Figure 17(b) that the concrete shotcrete layer does not crack and fall off, and the support effect is good.

5. Conclusion

(1) The larger the rise-span ratio, the greater the yield load and ultimate bearing capacity of the CFST circular arch specimen and the stronger the deformation resistance of circular arch. Compared with CFST circular arch specimens with a rise-span ratio of 0.154, the yield load of specimens with a rise-span ratio of 0.207 and 0.26 is increased by more than 1.5 times, and the ultimate bearing capacity is increased by 42.7% and 68.3%, respectively. The bearing capacity is significantly affected by the rise-span ratio.

(2) The larger the rise-span ratio, the higher the deformation degree of the specimen. When reaching the ultimate bearing capacity, the circular arch can produce large deformation and have a long yield stage with superior ductility. The deformation leads to the redistribution of internal force, the bending moment at the arch foot decreases, and the maximum bending moment appears in the middle of the span or near 1/4 of the span.

(3) The failure mechanism of circular arch under six-point uniformly distributed load is expounded. The internal force of specimens with different rise-span ratios is not evenly distributed, and the bending moment and axial force change obviously in the local area under load. In the elastic deformation stage, the maximum values of bending moment and axial force are generated at the arch foot. The core concrete at the arch foot is damaged by shear crushing and expansion under the action of compression and bending, resulting in expansion deformation. After the steel pipe yields, the circular section cannot be maintained, the restraint effect on the concrete is weakened, the deformation at the arch foot is increased, and the curvature of the whole specimen is inconsistent. As a result, the load is further increased and the failure of the bearing performance of the specimen is eventually caused.

(4) Based on the analysis of the actual deformation characteristics of the surrounding rock of the temporary sump in the roadway, its application requirements are considered, and a closed composite support scheme of "bolt mesh shotcrete + vertical elliptical CFST support + steel fiber concrete shotcrete layer + reinforced anchor cable" is proposed, which has been successfully applied in a coal mine.

Data Availability

The data used to support the findings of this study are available from the corresponding author upon request.

Conflicts of Interest

The authors declare no conflicts of interest.

Acknowledgments

This study was supported by the National Natural Science Foundation of China (no. 51904149) and the Shandong Provincial Natural Science Foundation, China (ZR2019BEE013).

References

[1] L.-H. Han, W. Li, and R. Bjorhovde, "Developments and advanced applications of concrete-filled steel tubular (CFST) structures: Members," *Journal of Constructional Steel Research*, vol. 100, pp. 211–228, 2014.

[2] L. H. Han, F. Y. Liao, Z. Tao, and Z. Hong, "Performance of concrete filled steel tube reinforced concrete columns subjected to cyclic bending," *Journal of Constructional Steel Research*, vol. 65, no. 8-9, pp. 1607–1616, 2009.

[3] Y. K. R. Gunawardena, F. Aslani, B. Uy, W.-H. Kang, and S. Hicks, "Review of strength behaviour of circular concrete filled steel tubes under monotonic pure bending," *Journal of Constructional Steel Research*, vol. 158, pp. 460–474, 2019.

[4] X. Han, D. Fernando, and B. Han, "Numerical modelling of the in-plane behaviour of concrete-filled circular steel tubular arches," *Construction and Building Materials*, vol. 264, Article ID 120693, 2020.

[5] Z. Tao and L.-H. Han, "Behaviour of fire-exposed concrete-filled steel tubular beam columns repaired with CFRP wraps," *Thin-Walled Structures*, vol. 45, no. 1, pp. 63–76, 2007.

[6] Z. Zhou, X. Cai, X. Li, W. Cao, and X. Du, "Dynamic response and energy evolution of sandstone under coupled static-dynamic compression: insights from experimental study into deep rock engineering applications," *Rock Mechanics and Rock Engineering*, vol. 53, no. 3, pp. 1305–1331, 2020.

[7] Q.-H. Tan, L. Gardner, L.-H. Han, and T.-Y. Song, "Performance of concrete-filled stainless steel tubular (CFSST) columns after exposure to fire," *Thin-Walled Structures*, vol. 149, Article ID 106629, 2020.

[8] B. Jiang, Q. Qin, Q. Wang, S. Li, and H. Yu, "Study on mechanical properties and influencing factors of confined concrete arch in underground engineering with complex conditions," *Arabian Journal of Geosciences*, vol. 12, no. 21, p. 662, 2019.

[9] S. Li, L.-H. Han, F.-C. Wang, and C.-C. Hou, "Seismic behavior of fire-exposed concrete-filled steel tubular (CFST) columns," *Engineering Structures*, vol. 224, Article ID 111085, 2020.

[10] Z.-B. Wang, Q. Yu, and Z. Tao, "Behaviour of CFRP externally-reinforced circular CFST members under combined tension and bending," *Journal of Constructional Steel Research*, vol. 106, pp. 122–137, 2015.

[11] S. C. Li, Q. Wang, B. Jiang, and M. He, "Modeling and experimental study of mechanical properties of confined concrete arch in complicated deep underground engineering," *International Journal of Geomechanics*, vol. 17, no. 6, pp. 1–14, 2016.

[12] W. Lu and H. Sun, "Study on support characteristic curve of concrete-filled steel tubular arch in underground support," *Structure*, vol. 27, pp. 1809–1819, 2020.

[13] Y. F. Gao, B. Wang, J. Wang, B. Li, and F. Xing, "Test on structural property and application of concrete-filled steel tube support of deep mine and soft rock roadway," *Chinese Journal of Rock Mechanics and Engineering*, vol. 29, no. S1, pp. 2604–2609, 2010, (in Chinese).

[14] J. Zhang, L. Liu, J. Cao, X. Yan, and F. Zhang, "Mechanism and application of concrete-filled steel tubular support in deep and high stress roadway," *Construction and Building Materials*, vol. 186, pp. 233–246, 2018.

[15] F. Q. Xia and J. Wang, "Supporting technology of flexural strengthened concrete-filled steel tube," *Journal of Mining & Safety Engineering*, vol. 37, pp. 490–497, 2020, (in Chinese).

[16] Y. F. Gao, K. M. Liu, S. W. Feng, W. Zhao, and G. L. Qu, "Early strength concrete experiment and applied research of early strength concrete-filled steel tubular supports in extremely soft rock roadways," *Journal of Mining & Safety Engineering*, vol. 32, pp. 537–543, 2015, (in Chinese).

[17] X. S. He, K. M. Liu, L. Zhang, and H. Guo, "Structural design and application of concrete-filled steel tube support at extremely soft rock roadway intersection," *Journal of China Coal Society*, vol. 40, pp. 2040–2048, 2015, (in Chinese).

[18] X. B. Li, R. S. Yang, Y. F. Gao, X. S. He, and C. Wang, "High-strength steel tubular confined concrete supports support technology for large section soft rock inclined shaft," *Journal of China Coal Society*, vol. 38, pp. 1742–1748, 2013, (in Chinese).

[19] X. B. Li, R. S. Yang, Y. F. Gao, and H. J. Xue, "Study on combined support technology of bolt-mesh-shotcrete and concrete filled steel tubular supports for soft rock roadway in Yangzhuang mine," *Journal of Mining & Safety Engineering*, vol. 32, pp. 285–290, 2015, (in Chinese).

[20] X. S. Kong, R. L. Shan, H. H. Yuan, Y. H. Xiao, X. S. He, and T. T. Bao, "Study on the sustaining effect of concrete-filled steel tubular supports in deep mining roadways," *Arabian Journal of Geosciences*, vol. 13, pp. 1–14, 2020.

[21] J. Wang, C. C. Hu, J. P. Zuo, B. Wang, and Q. F. Mao, "Mechanism of roadway floor heave and control technology in fault fracture zone," *Journal of China Coal Society*, vol. 44, pp. 397–408, 2019.

[22] D. Liu, J. Zuo, J. Wang et al., "Bending failure mechanism and strengthening of concrete-filled steel tubular support," *Engineering Structures*, vol. 198, Article ID 109449, 2019.

[23] D. J. Liu, J. P. Zuo, S. Guo, J. Wang, Y. J. Li, and T. L. Zhang, "Research on load-bearing ability of steel tube confined concrete supports for deep roadway: state of the art," *Journal of China University of Mining &.Technology*, vol. 47, pp. 1193–1211, 2018, (in Chinese).

[24] X. B. Li, *Steel Tube Confined concrete Strength and the Roadway Compression Ring Enhanced Support Theory*, China University Of Mining And Technology- BeiJing, Beijing, China, 2012.

[25] J. Wang, *Flexural Mechanical Properties experiment and Application Research of Concrete-filled Steel Tube Beam and Arch*, China University Of Mining And Technology- BeiJing, Beijing, China, 2014.

[26] G. L. Qu, *Research on Flexural Performance of Concrete-filled Steel Tubular Support and its Application*, China University Of Mining And Technology-BeiJing, Beijing, China, 2013.

[27] G. L. Liu, *Research on Steel Tube Confined Concrete Supports Capability and Soft Rock Roadway Compression Ring Strengthening Supporting Theory*, China University Of Mining And Technology-BeiJing, Beijing, China, 2013.

[28] X. S. He, *Research on Application and Behavior of Concrete-Filled Steel Tubes Arch under Bending State*, China University Of Mining And Technology-BeiJing, Beijing, China, 2016.

[29] X. B. Li, Y. F. Gao, R. S. Yang, G. L. Qu, X. S. He, and H. J. Xue, "Mechanical performance testing and analysis of steel tuber confined concrete supports in roadway supporting," *Journal of Mining & Safety Engineering*, vol. 30, pp. 817–821, 2013, (in Chinese).